Research on Chemical Intermediates (2025) 51:4149–4176
https://doi.org/10.1007/s11164-025-05652-y

Outperformance of CaO-incorporated alumina-supported Pd catalysts in methanol decomposition

Busra Eryildirim[1] · Nuray Oktar[2] · Doruk Dogu[3]

Received: 17 March 2025 / Accepted: 25 May 2025 / Published online: 27 June 2025

Abstract

This study aimed to investigate the impact of CaO incorporation to alumina-supported Pd catalysts on the methanol decomposition reaction. For this purpose, mayenite, alumina and/or calcium oxide-supported Pd catalysts were synthesized. The synthesized catalysts were characterized by XRD, FTIR, Laser Raman spectroscopy, N_2 adsorption–desorption, pyridine adsorbed DRIFTS, CO_2-TPD, XPS, SEM–EDS, and ICP-OES techniques. Catalytic activity tests were carried out over a 6 h reaction period in the range of 100–400 °C. The results of the characterization and activity tests showed that the addition of CaO had significant effects on the physicochemical properties of the catalyst as well as on the catalytic activity. By adding CaO to the alumina support material, the acidity was reduced, thus reducing the selectivity for dimethyl ether (DME) formation, which is significantly high for the 1Pd@Al_2O_3 catalyst, and increasing the H_2 and CO selectivity. The mayenite-supported catalyst (1Pd@SGM), which contains alumina and calcium oxide in its unique crystal structure, showed an excellent catalytic performance close to complete methanol conversion with DME selectivity below 1% at 400 °C. In the stability test carried out at 350 °C for 6 h with 1Pd@Al_2O_3, 1Pd@SGM, and 1Pd@48CaO@Al_2O_3 catalysts used in the temperature scan, it was concluded that all catalysts were stable and 1Pd@SGM catalyst showed higher catalytic activity than the others.

✉ Nuray Oktar
nurayoktar@gazi.edu.tr

Busra Eryildirim
busra_eryildirim@hotmail.com

Doruk Dogu
doruk.dogu@atilim.edu.tr

[1] Department of Chemical Engineering, Graduate School of Natural and Applied Sciences, Gazi University, Ankara, Turkey

[2] Department of Chemical Engineering, Faculty of Engineering, Gazi University, Ankara, Turkey

[3] Department of Metallurgical and Materials Engineering, Atılım University, Ankara, Turkey

Graphical abstract

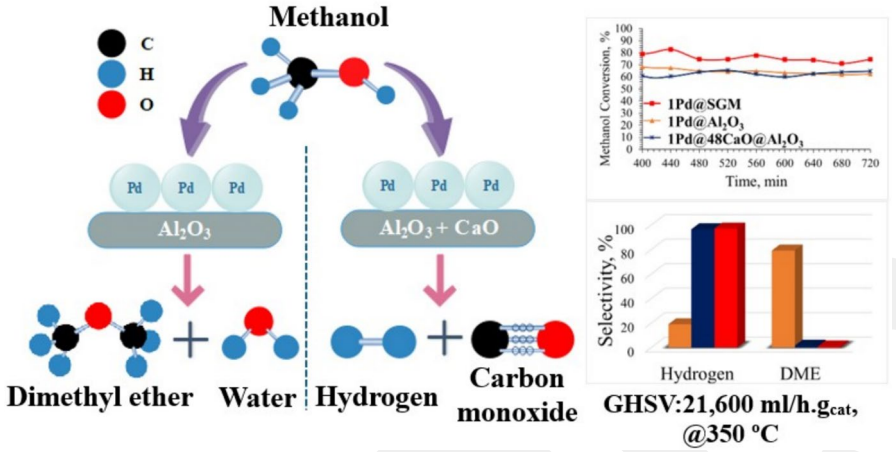

Keywords Hydrogen · Methanol decomposition · Mayenite · Alumina · Calcium oxide addition · Palladium

Introduction

Global energy need is expected to increase by 1.3% each year until 2040. The need for clean energy has been increasing with the increase in the world population, global economic growth, and the development of technology. Fossil fuels (natural gas, oil, coal), which are widely used for energy production, contribute significantly to global climate change by causing greenhouse gas emissions [1]. Hence, significant research has been directed to the development of renewable, clean, and environmentally friendly energy carriers. Hydrogen has a remarkable energy potential with three times the energy output of diesel and gasoline, and it can be used in many practical areas such as fuel cell technologies and internal combustion engines [2, 3]. When hydrogen is used to produce energy, only energy and water vapor are produced, so no greenhouse gases are released into the atmosphere. Hydrogen is considered an important energy vector of the future; however, safe storage and transportation of hydrogen at tolerable cost is a major challenge [4, 5]. In addition, hydrogen is not found in free form in nature and must be obtained by converting other chemicals. A feasible solution to these problems is to release the required amount of hydrogen from a stable hydrogen-containing liquid or solid in situ [6]. There are numerous processes for producing hydrogen from various materials such as water, alcohols, hydrocarbons, and biomass. Different methods such as steam reforming, dry reforming, electrolysis, and photocatalytic reactions are used in these processes [7, 8].

Methanol, a widely used basic chemical, is currently used in producing industrial raw materials (such as olefins and aromatics) and biofuels, and it can also be

used as an alternative to gasoline [9, 10]. Methanol is not only known as one of the most widely used chemicals, but it is also an excellent carrier of hydrogen due to its simple molecular structure, high energy content, low cost, safe transportation, and easy storage [11–16]. Most importantly, sustainable biomass and its reserves can be used to produce methanol, making it a non-fossil fuel-dependent energy carrier [17]. Due to these properties, hydrogen production from methanol has been accepted as an alternative to other processes. Four major processes exist to produce hydrogen from methanol: methanol decomposition (Eq. 1), methanol partial oxidation (Eq. 2), methanol steam reforming (Eq. 3), and autothermal reforming of methanol (Eq. 4) [18–21].

$$CH_3OH \leftrightarrow CO + 2H_2 \ \Delta H^{\circ}_{298} = +91 \text{ kJ mol}^{-1} \quad (1)$$

$$CH_3OH + 1/2O_2 \leftrightarrow CO_2 + 2H_2 \ \Delta H^{\circ}_{298} = -192 \text{ kJ mol}^{-1} \quad (2)$$

$$CH_3OH + H_2O \leftrightarrow CO_2 + 3H_2 \ \Delta H^{\circ}_{298} = +50 \text{ kJ mol}^{-1} \quad (3)$$

$$CH_3OH + (1-2x)H_2O + xO_2 \leftrightarrow CO_2 + (3-2x)H_2 \ \Delta H^{\circ}_{298} = -242(2x) + 50 \text{ kJ mol}^{-1} \quad (4)$$

Among these reactions, partial oxidation of methanol is an exothermic reaction that can easily lead to the deactivation of catalysts. Reforming reactions are more complex processes. Methanol decomposition carried out at lower temperatures provides an economic advantage and operational convenience over methanol reforming [12, 17, 22]. Interest in methanol decomposition is increasing due to the possibility of using methanol as an onboard hydrogen source for fuel cells, as well as the possibility of using it as a source of synthesis gas [23]. The main products formed by the decomposition of methanol are hydrogen and carbon monoxide. However, conditions such as catalyst composition and reaction temperature can cause the formation of undesired products due to the side reactions, reducing the selectivity for hydrogen and carbon monoxide formation. The by-products formed during the decomposition of methanol are dimethyl ether (DME), methane, carbon dioxide, methyl formate, formaldehyde, and formic acid [23]. DME is formed due to the methanol dehydration reaction (Eq. 5). Methyl formate, which is formed due to methanol dehydrogenation (Eq. 6), combines with water to form formic acid (Eq. 7). Formaldehyde is formed by the decomposition of methanol into hydrogen and formaldehyde (Eq. 8).

$$2CH_3OH \leftrightarrow CH_3OCH_3 + H_2O \ \Delta H^{\circ}_{298} = -24\text{kJ mol}^{-1} \quad (5)$$

$$2CH_3OH \leftrightarrow HCOOCH_3 + 2H_2 \ \Delta H^{\circ}_{298} = +4\text{kJ mol}^{-1} \quad (6)$$

$$HCOOCH_3 + H_2O \leftrightarrow CH_3OH + HCOOH \ \Delta H^{\circ}_{298} = +14\text{kJ mol}^{-1} \quad (7)$$

$$CH_3OH \leftrightarrow HCHO + H_2 \ \Delta H^{\circ}_{298} = +92\text{kJ mol}^{-1} \quad (8)$$

Methane, another important by-product of methanol decomposition, is formed by the methanation reaction (Eq. 9). One possible mechanism of CO_2 formation could be due to the water gas shift reaction (Eq. 10) or the Boudouard reaction (Eq. 11). The coke formed by the Boudouard reaction can lead to catalyst deactivation and reactor clogging. Therefore, it is critical to develop an active catalyst that is resistant to coke formation.

$$CO + 3H_2 \leftrightarrow CH_4 + H_2O \ \Delta H^{\circ}_{298} = -206\text{kJ mol}^{-1} \quad (9)$$

$$CO + H_2O \leftrightarrow H_2 + CO_2 \ \Delta H^{\circ}_{298} = -41\text{kJ mol}^{-1} \quad (10)$$

$$2CO \leftrightarrow C + CO_2 \ \Delta H^{\circ}_{298} = -172\text{kJ mol}^{-1} \quad (11)$$

The catalytic performances of various metals were studied in the literature for their methanol decomposition activity. These metals can be classified into Cu-based catalysts, such as $CuAl_2O_4$ [6], Cu/Zn/Ni [11], Cu–ZnO [24], Cu/SiO_2 [25], and Group VIII B elements such as Ru [13], Ni [26–29], Pt [30–34], Pd [22, 35–38]. Copper-based catalysts have attracted wide research interest since copper is inexpensive and exhibits excellent catalytic activity at lower reaction temperatures; however, Cu-based catalysts have some disadvantages, such as deactivation due to blockage or sintering of active sites, which can occur at high temperatures [39]. In addition, for Cu-catalysts at temperatures below 250 ºC, selectivity to the syngas is not sufficient due to the formation of methyl formate [40]. Due to the instability problems of the Cu-based catalysts in the methanol decomposition reaction, research on other active metals gained more interest. Pd-based catalysts show better thermal stability above 200 °C for methanol decomposition than Cu-based catalysts [22]. Compared to conventional hydrogen production techniques, the use of Pd-based catalysts for methanol decomposition offers several benefits. First, compared to alternative methods, the reaction may be conducted at lower temperatures, which lowers energy consumption and boosts process efficiency. Second, the reaction's selectivity for producing hydrogen is enhanced, reducing the formation of undesired byproducts [36].

The effect of the catalyst support material is also very important in terms of catalytic performance and product selectivity. The active metals used for methanol decomposition are supported on various oxides such as MgO [23], Al_2O_3 [31, 41], ZrO_2 [37, 42], SiO_2 [25, 27, 28], CeO_2 [30, 36, 39], TiO_2 [43]. The properties of the catalyst support directly affect product selectivity. DME, which can be formed due to methanol dehydration, reduces the hydrogen and carbon monoxide selectivity. Since ether formation is favored in acidic environments, DME formation increases in the presence of more acidic catalysts [44, 45]. By reducing the acidity in the catalyst used, the dehydration of methanol and DME formation can be suppressed, and H_2 and CO selectivity increases. The acidity of the catalysts can be reduced by adding alkaline elements such as Na, K, and Li to their structure [6, 46].

The main objective of the present study is to investigate the effects of adding Ca, which is an alkali element, to alumina support material on methanol decomposition. For this purpose, commercial γ-Al_2O_3 and/or CaO-supported Pd-containing catalysts were synthesized by the wet impregnation method, and their catalytic performances were compared in methanol decomposition. It is also thought that mayenite ($Ca_{12}Al_{14}O_{33}$, $12CaO.7Al_2O_3$), which is a type of mineral consisting of 48.53% CaO and 51.47% Al_2O_3 by mass, might be a promising support material for methanol decomposition. To our knowledge, no study has been reported using mayenite as a support material in methanol decomposition previously. It has been reported that mayenite exhibits high activity as a support material in catalytic studies such as partial oxidation of methane [47], dry reforming of CH_4 [48], biomass tar cracking [49], and steam reforming of biogas [50]. This study reveals that mayenite support materials can be effective for methanol decomposition as well. In the study, mayenite was synthesized by the citrate sol–gel method. The physical and structural properties of the catalysts used were evaluated regarding product selectivity, especially according to the surface acidity-basicity effect. It has been determined that the properties of the support material used are of great importance in terms of product selectivity in methanol decomposition.

Experimental

Preparation of catalysts

In this study, commercial gamma alumina (SA 6*73) supplied from Saint Gobain, and commercial calcium oxide (12047) from Sigma Aldrich were used in addition to the mayenite supports synthesized in-house. Alumina was calcined at 800 °C with dry air flow for 6 h, and calcium oxide was calcined at 900 °C for 4 h in a muffle furnace before being used in the synthesis.

Mayenite material was synthesized using a citrate sol–gel method [51]. Calcium nitrate tetrahydrate ($Ca(NO_3)_2.4H_2O$, Merck) and aluminum nitrate tetrahydrate ($Al(NO_3)_3.9H_2O$, Merck) were used as the starting materials for this synthesis. The citric acid ($C_6H_8O_7$, Sigma-Aldrich) was used as a chelating agent and ethylenediamine ($C_2H_4(NH_2)_2$, Sigma-Aldrich) was used for pH adjustment. Starting materials were mixed with the determined molar ratio (Ca/Al:12/14) and dissolved in deionized water. Then, the solution was stirred and heated to 60 °C. Citric acid (metal salts/citric acid (MS/CA) molar ratio is 1/2) was added to this solution, and the solution's pH was adjusted to 2 with ethylenediamine. The solution was heated to 85 °C under continuous stirring with a magnetic stirrer and vigorously stirred at 85 °C until a gel was formed. The resulting gel was then dried at 130 °C for 12 h to form a cake-like structure. Finally, the dried product was heated from room temperature to 1200 °C at a heating rate of 5 °C/min and calcined at 1200 °C under a dry airflow in a tubular furnace for 4 h. The final product is called SGM (sol–gel mayenite).

Mayenite, calcium oxide and/or alumina-supported Pd catalysts were prepared by the wet impregnation method. The Pd content of all catalysts is set as 1wt%. Palladium (II) nitrate hydrate ($Pd(NO_3)_2{\cdot}xH_2O$, Sigma-Aldrich) was used as the Pd

precursor. In the synthesis, the support material was initially dispersed in deionized water at 40 ºC. The metal source was also dissolved in deionized water and this solution was added dropwise to the solution containing the support material while stirring. After impregnation, water was removed by evaporation, and the remaining solid was calcined under dry air at 500 ºC for 4 h. Catalyst naming is expressed as "weight percent metal content@support material name"; as 1Pd@Al_2O_3, 1Pd@CaO, and 1Pd@SGM. To investigate the effect of calcium oxide on the alumina support, a catalyst containing equal weight ratios of alumina and calcium oxide was also synthesized. For this, the support of the Pd-impregnated catalyst containing an equal amount of calcium oxide and alumina was physically mixed and the material was calcined at 500 °C for 4 h under dry air flow. The obtained catalyst was named 1Pd@Al_2O_3–CaO. The effect of calcium on the reaction was also investigated by adding calcium oxide to alumina by wet impregnation method. While determining the amount of calcium oxide to be loaded, the calcium oxide ratio in the mayenite content was taken into consideration. First, 48% CaO (as source $Ca(NO_3)_2.4H_2O$, Merck) by mass was added to the alumina support material by wet impregnation procedure. The material was then calcined in a muffle furnace at 900 ºC for 4 h. 1 wt% Pd was added to the obtained material by wet impregnation procedure as explained above and was calcined under dry air at 500 ºC for 4 h. This catalyst was named as 1Pd@48CaO@Al_2O_3. Synthesized Pd-containing catalysts were reduced under a hydrogen flow at 400 ºC for 1 h before the activity tests. Table 1 summarizes the catalysts prepared within the study and the synthesis method.

Characterization of the synthesized catalysts

Synthesized catalysts were characterized by X-ray diffraction (XRD), N_2 adsorption–desorption, Fourier-transform infrared spectroscopy (FTIR), pyridine adsorbed diffuse reflectance Fourier transformed infrared spectroscopy (DRIFTS), carbon dioxide—temperature programmed desorption (CO_2-TPD), Laser Raman spectroscopy, X-ray photoelectron spectroscopy (XPS), inductively coupled plasma-optical emission spectrometry (ICP-OES), and scanning electron microscopy-energy dispersive X-ray spectroscopy (SEM–EDS). All characterization techniques were applied to reduced catalysts.

X-ray diffraction analysis was performed using a Bruker D2 Phaser diffractometer with a Cu, K_α ($\lambda = 0.15406$ nm) radiation source to determine the crystal structure

Table 1 Synthesized catalysts and their preparation method

Catalyst	Support	Support preparation method	Catalyst preparation method
1Pd@Al_2O_3	Al_2O_3	Commercial	Wet impregnation
1Pd@CaO	CaO	Commercial	Wet impregnation
1Pd@Al_2O_3–CaO	Al_2O_3–CaO	Physical mixing	Wet impregnation
1Pd@SGM	$12CaO{\cdot}7Al_2O_3$	Citrate sol–gel	Wet impregnation
1Pd@48CaO@Al_2O_3	48CaO@Al_2O_3	Wet impregnation	Wet impregnation

of the synthesized catalysts. The scanning range of 2θ was 10–90º with a scanning speed of 2°/min.

Nitrogen adsorption–desorption analysis was conducted for the surface area and porosity properties of the synthesized catalysts. Analysis was performed using a Micromeritics Tristar II 3020 device at 77 K within P/Po values of 10^{-5}-0.99. Before the analysis, all materials were degassed under high vacuum conditions at 250 °C for 2 h.

FTIR and DRIFTS studies were performed using a JASCO Model FT/IR-4700 instrument. FTIR analysis was carried out to determine the functional groups and bonds in the catalyst structure, and DRIFTS analysis was carried out to determine the surface acidities. For DRIFTS analysis, a small amount of pyridine is dropped onto the sample whose surface acidity is to be determined, and the sample is kept in the oven at 40 °C for 2 h. DRIFTS spectra of pyridine adsorbed samples are taken and the acidic structure of the catalyst is determined after taking the difference between the spectrum of the pyridine adsorbed sample and the fresh sample.

The CO_2-TPD analysis was performed to determine the basic sites over the synthesized catalysts. For the analysis, a 0.05 g catalyst was placed in the center of the quartz tubular reactor and supported with quartz wool. The quartz reactor, which had an internal diameter of 6 mm, was placed in a tubular electrical furnace, and the temperature was controlled by the temperature controller (Ordel AC441). The reduced catalyst was preheated from room temperature to 500 ºC at a heating rate of 10 ºC/min and kept at 500 ºC for 1 h under a He flow (30 sccm) initially to remove contaminants from the surface. After that, the catalyst was cooled down to 50 ºC, and pure CO_2 (30 sccm) flow was introduced into the reactor for 1 h. The reactor was then purged with He for 2 h before the CO_2 desorption analysis. The catalyst was finally heated from 50 to 900 ºC at a heating rate of 10 ºC/min under 30 sccm flow of He to detect the amount of the desorbed CO_2. Throughout the experiment, mass signal 44 was monitored by an MKS Cirrus atmospheric pressure gas analyzer fed from the reactor's gas outlet.

A JASCO NRS4500 Raman Spectrometer equipped with a 532 nm ion laser was used to conduct laser Raman Spectroscopy analyses at room temperature. To determine the surface chemistry of the catalysts, an XPS analysis was performed with a PHI 5000 VersaProbe device. XPSPEAK41 software was used for curve fitting. The binding energies for the Pd region were corrected by referencing the C 1s spectra at 284.5 eV.

SEM–EDS analysis was performed with a HITACHI SU5000 Field Emission scanning electron microscope to determine the morphology and metal contents of the synthesized materials. Metal ratios of synthesized catalysts were also determined by ICP-OES analysis with a PerkinElmer Optima 4300DV instrument.

Activity tests of the synthesized catalysts

Catalytic performances of the synthesized catalysts were tested for the methanol decomposition reaction. The activity test system consists of three main sections: the section where the feed gas mixture is prepared, the temperature-controlled tube

furnace section, where the reaction takes place at a constant temperature, and the section where the gas chromatography device is located, where the analysis of the reactant and resulting products is carried out. The schematic representation of the experimental system is given in Fig. 1. Activity tests were carried out in a quartz tubular flow reactor, having an inner diameter of 8 mm, which was placed in a tubular electrical furnace (Protherm). The reactor's temperature was controlled by the Honeywell DC1020 temperature controller, with an accuracy of 99.5%. All Pd-containing catalysts were reduced under H_2 flow at 400 ºC for 1 h before the activity tests. The reduced catalyst was pelletized and cut into small pieces and then the catalyst was loaded into the reactor tube and supported from both ends by quartz wool. The particle size range of the catalyst was 1–2 mm and 0.1 g catalyst was used in each test. In the system, methanol was fed to the evaporator (150 °C) in the liquid phase with the help of a syringe pump, and a mass flow meter was used to adjust the gas flow rate. The lines were heated to 150 °C with the help of heating tapes to prevent condensation. Argon was used as the carrier gas and the feed gas mixture was fed to the reactor at a total rate of 36 ml/min (Methanol/Argon: 1/5, GHSV: 21,000 ml/h.g_{cat}). Reactions were carried out in the temperature range of 100–400 °C, considering the hydrogen production studies from methanol [30–39]. A gas chromatograph was used to analyze the product stream leaving the reactor, which was connected online to the reactor exit stream. Chromatograms against time are taken from the gas chromatograph every 25 °C in temperature scanning studies, and every forty minutes in constant temperature studies. The system used an Agilent 6890 N Gas Chromatograph device, which includes a thermal conductivity detector (TCD), flame ionization detector (FID), Propak-S, and HP-Plot Q column. H_2, CO, CH_4, and CO_2 gases were analyzed with the TCD, and C_2H_6O, CH_3OH, CH_2O_2, and CH_2O gases were analyzed with the FID. The catalytic activity test results were evaluated in terms of methanol conversion (Eq. 12) and product selectivities (Eq. 13–15).

$$\text{CH}_3\text{OH Conversion (\%)}: X_{CH_3OH} = \frac{(\text{moles } CH_3OH_{in} - \text{ moles } CH_3OH_{out})}{\text{moles } CH_3OH_{in}} \times 100 \quad (12)$$

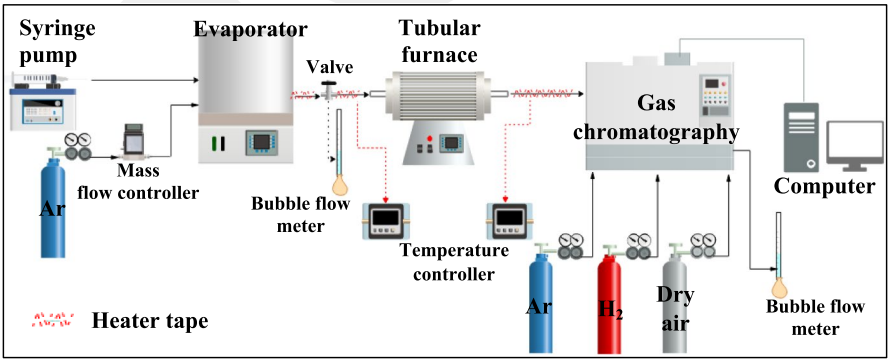

Fig. 1 A schematic diagram of activity testing system

$$\text{Selectivity to } H_2\ (\%):\ S_{H_2} = \frac{{}^1/_2 \times \text{ moles } H_2}{(\text{moles } CH_3OH_{in} - \text{moles } CH_3OH_{out})} \times 100 \tag{13}$$

$$\text{Selectivity to } C_2H_6O\ (\%):\ S_{C_2H_6O} = \frac{2 \times \text{ moles } C_2H_6O}{(\text{moles } CH_3OH_{in} - \text{ moles } CH_3OH_{out})} \times 100 \tag{14}$$

$$\text{Selectivity to CO, } CH_4, CO_2, CH_2O_2, CH_2O\ (\%):\ S_i = \frac{\text{moles } i}{(\text{moles } CH_3OH_{in} - \text{ moles } CH_3OH_{out})} \times 100 \tag{15}$$

Results and discussion

Characterization of the synthesized catalysts

The XRD patterns (2θ range of 10–90°) of the pure support materials and synthesized Pd-containing catalysts were given in Fig. 2a,b. The phases of the synthesized materials were identified by the "DIFFRAC.EVA" program, which is the software of the Bruker D2 Phaser diffractometer. Results were also confirmed by the literature. Pure alumina and $1Pd@Al_2O_3$ catalyst showed the characteristic peaks of γ-Al_2O_3 at 2θ values of 19.3°, 32.8º, 37.5º, 39.7º, 45.29°, 60.6° and 67.1º (JCPDS Card No: 26–0093) [52–54]. Commercial CaO catalyst after calcination showed

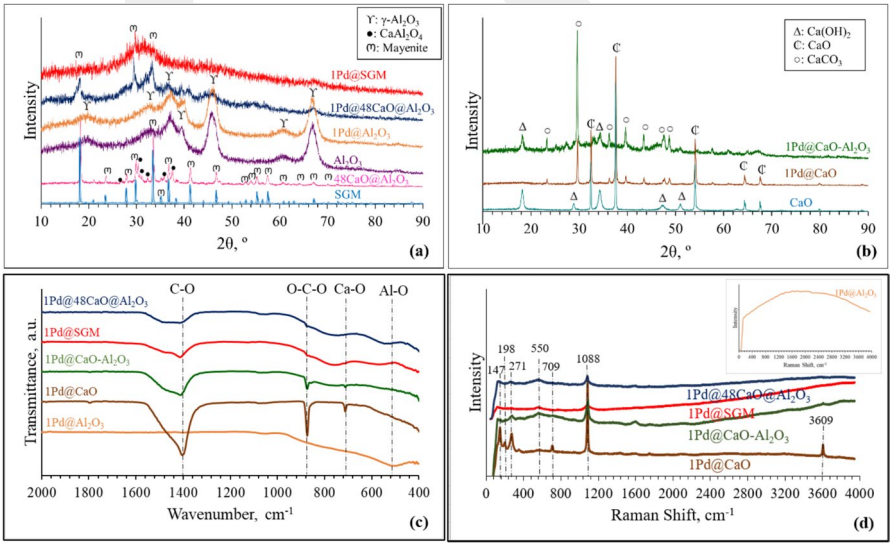

Fig. 2 (**a**) XRD pattern for SGM and Al_2O_3 supported Pd catalysts, (**b**) XRD pattern for CaO and Al_2O_3 supported Pd catalysts, (**c**) FTIR spectra of the synthesized reduced catalysts, and (**d**) Raman spectra of the synthesized reduced catalysts

CaO (2θ: 32.3°, 37.5°, 54°, 64.3°, 67.6°, lime, COD 1000044 and JCPDS Card No: 00–037–1497 [55]) and $Ca(OH)_2$ (2θ: 18.1°, 28.8°, 34.2°, 47.4°, 50.9°, portlandite, COD 9009098 and JCPDS Card No: 00–004–0733 [55]) phases in its structure (Fig. 1b). After adding palladium to the structure, the $CaCO_3$ phase (2θ: 23.4°, 29.7°, 31.6°, 36.3°, 39.7°, 43.2°, 43.4°, 47.3°, 47.7°, 48.8°, 57.7°, 61°, 65°, calcite, COD 9000965 and JCPDS Card No 00–009–0035) was also observed in the crystal structure of the 1Pd@CaO and 1Pd@CaO–Al_2O_3 catalysts obtained. The $CaCO_3$ phase found is thought to be related to the atmospheric carbonation reaction. CaO is known and widely used as a good sorbent in CO_2 capture processes and the $CaCO_3$ phase can easily occur in the presence of CaO and trace amounts of CO_2 in the atmosphere [56–60]. Although atmospheric CO_2 is the most likely candidate for carbonation of CaO, it should be noted that any possible carbon-containing impurities present during the impregnation process may also contribute to formation of $CaCO_3$.

The XRD pattern of sol–gel synthesized mayenite shows its main characteristic peaks around 2θ: 18.1°, 30°, 33.4°, 36.7°, 41.2°, 46.7°, 55.2° and 57.4° (COD 2102955 and JCPDS Card No: 70–2144 [61]). It has been observed that there is a change in the crystal structure after impregnation of palladium on the support material and the mayenite structure is distorted (Fig. 2a). The amount of calcium oxide in the 48CaO@Al_2O_3 is set to be the same as the content of mayenite. The XRD analysis of this material also showed small amounts of the $CaAl_2O_4$ phase (2θ: 30.54°, 32.10°, 35.53°, 37.26°, COD 4308075 and JCPDS Card No: 53–0191 [62]) together with the mayenite phase. As in the mayenite support, a change occurred in the crystal structure of the 48CaO@Al_2O_3 with the palladium impregnation (Fig. 2a). In the XRD analysis of all Pd-impregnated catalysts, no Pd peaks were observed. This is thought to be due to the small crystal size of palladium.

The results of FTIR analysis performed to determine the bond structures of the synthesized catalysts are given in Fig. 2c. The band at ~ 510 cm^{-1} wavenumber in the FTIR spectra of the 1Pd@Al_2O_3 catalyst belongs to the Al–O stretching mode bond. This is the band seen in the characteristic structure of γ-Al_2O_3 [54]. The bands at around 1400 and 872 cm^{-1} in the 1Pd@CaO catalyst were associated with the stretching vibrations of C–O and O–C–O stretching modes, respectively. These bands emerged possibly due to the reaction of catalysts with CO_2 in the air forming $CaCO_3$ during the sample preparation. The $CaCO_3$ phases seen in the XRD pattern (Fig. 2b) also confirm this result. The band at 712 cm^{-1} can be assigned to the Ca–O bond expected in the CaO structure [63–66]. The FTIR spectrum of the 1Pd@CaO–Al_2O_3 catalyst is similar to the 1Pd@CaO catalyst spectrum. In addition, FTIR spectra of 1Pd@SGM and 1Pd@48CaO@Al_2O_3 catalysts, similar to XRD patterns, show similar characteristics. In these catalysts, bands in the 700–400 cm^{-1} range were related to the bonds of Ca, Al, and O atoms [67].

The results of the phase identities of the synthesized catalysts were also supported by Raman analysis in addition to XRD and FTIR. The obtained Raman spectra are given in Fig. 2d. No mode was observed in the Raman spectra of the 1Pd@Al_2O_3 catalyst in the 100–4000 cm^{-1} range. The support material γ-Al_2O_3 is reported not to show any Raman transition [68–70]. PdO is a very Raman-active oxide and shows modes in the Raman spectrum in the range of 200–1300 cm^{-1} [71]. The absence of any modes in the 1Pd@Al_2O_3 catalyst shows that there is no PdO in the structure

and this result is later confirmed with XPS analysis. The pure CaO molecule does not exhibit any first-order Raman active modes [72]. The Raman modes of the 1Pd@CaO observed at 147, 271, 709, and 1088 cm^{-1} are attributed to the $CaCO_3$ phase, and the vibrations seen in the regions around 198 and 3609 cm^{-1} are attributed to the vibrations of $Ca(OH)_2$ [59, 73]. This result is also in agreement with the XRD and FTIR analyses. The XRD pattern and the FTIR spectra of the catalyst have peaks of $CaCO_3$ and $Ca(OH)_2$ phases. The modes seen at approximately 270 and 1090 cm^{-1} in calcium oxide and alumina-supported materials belong to the $CaCO_3$ phase. This phase was also determined in the FTIR spectra of 1Pd@CaO–Al_2O_3, 1Pd@SGM, and 1Pd@48CaO@Al_2O_3 catalysts. The reason why the $CaCO_3$ phase, which is clearly determined in the XRD pattern of the 1Pd@CaO–Al_2O_3 catalyst, is not seen in the 1Pd@SGM and 1Pd@48CaO@Al_2O_3 catalysts may be because of the small crystal size. The presence of $CaCO_3$ and $Ca(OH)_2$ phases in calcium-containing materials is not surprising because CaO is highly reactive and can form these phases upon exposure to ambient air during storage [59]. The mode observed at around 550 cm^{-1} in the aluminum-containing materials is associated with the presence of Al–O–Al bridges [74, 75]. These conclusions supported the XRD and FTIR analysis results of the synthesized reduced catalysts.

The results of N_2 adsorption–desorption analysis performed to obtain surface area and porosity information of the synthesized materials are given in Fig. 3 and Table 2. The isotherms obtained for 1Pd@Al_2O_3 and 1Pd@CaO–Al_2O_3 catalysts are consistent with Type IV and show H1-type hysteresis (Fig. 3a). Type IV isotherm is a characteristic feature of mesoporous materials. H1-type hysteresis is

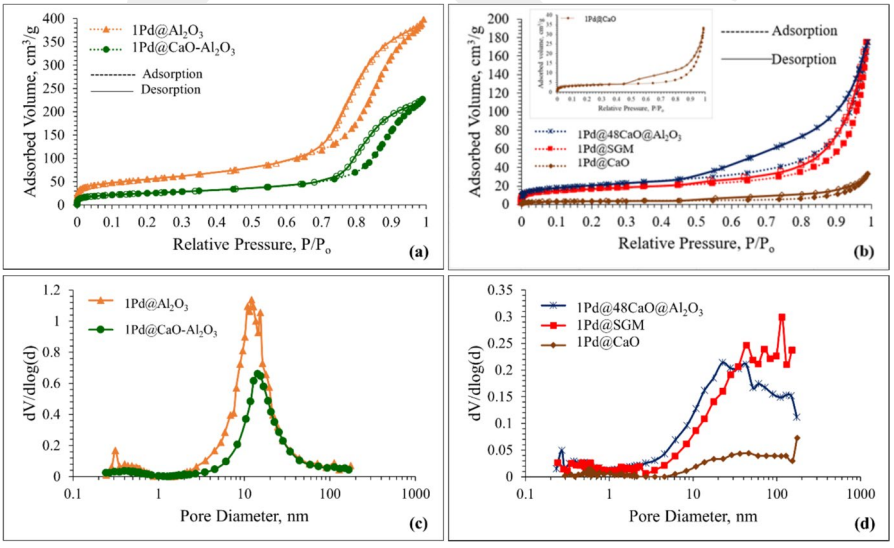

Fig. 3 N_2 adsorption–desorption analysis results (**a**) N_2 adsorption–desorption isotherms of the reduced 1Pd@Al_2O_3 and 1Pd@CaO–Al_2O_3 catalysts, (**b**) N_2 adsorption–desorption isotherms of the reduced 1Pd@SGM, 1Pd@CaO, and 1Pd@48CaO@Al_2O_3 catalysts, (**c**) pore distribution of the reduced 1Pd@Al_2O_3 and 1Pd@CaO–Al_2O_3 catalysts, and (**d**) pore distribution of the reduced 1Pd@SGM, 1Pd@CaO, and 1Pd@48CaO@Al_2O_3 catalysts

Table 2 The physical and chemical properties of the synthesized catalysts

Material	Nominal chemical composition, wt.% Pd	ICP-OES results, wt.% Pd	EDS results, wt.% Pd	Multi point BET surface area, m^2/g	BJH adsorption average pore diameter, nm	Pore volume, cm^3/g
1Pd@Al_2O_3	1	0.75 ± 0.02	0.7	189.83	4.74	0.62
1Pd@CaO	1	0.58 ± 0.04	1	11.56	6.84	0.05
1Pd@CaO–Al_2O_3	1	0.71 ± 0.04	0.8	87.34	5.72	0.35
1Pd@SGM	1	0.70 ± 0.04	0.8	55.43	6.16	0.27
1Pd@48CaO@Al_2O_3	1	0.79 ± 0.02	1.5	69.62	5.23	0.27

generally associated with well-defined cylinder-like pore spaces or agglomeration of regular spherical particles [8]. These materials show a uniform distribution in the pore distribution, as shown in Fig. 3c. The surface area of commercial Al_2O_3 is reported as 200 m^2/g [1], the surface area is observed due to metal migration within the pore structure of the material. The isotherms of 1Pd@SGM, 1Pd@CaO, and 1Pd@48CaO@Al_2O_3 catalysts are compatible with Type II and have H3-type hysteresis (Fig. 3b). Type II isotherm is the characteristic isotherm obtained with non-porous or macroporous materials and represents unlimited single-layer-multilayer adsorption. H3-type hysteresis is an indication that there is no adsorption limitation on the material at high P/P_o values and that the material contains plate-shaped particles and slit-shaped pores. It is also known that open macropores are present in materials with this type of hysteresis. The pore distribution graph shows that these materials have microporous structures (Fig. 3d). The surface area of pure mayenite is less than 5 m^2/g, and there is a significant increase in surface area since the structure cannot be fully protected by impregnation of Pd into the structure.

Determination of the acidity of the catalyst used in the methanol decomposition reaction is essential for product selectivity. Since ether formation is favored in an acidic medium, the selectivity of DME, an important by-product in the methanol decomposition reaction, increases in the presence of acidic sites. The increase in DME selectivity would lead to decreased hydrogen selectivity [6, 46]. DRIFTS analyses of pyridine-adsorbed samples were performed to determine the surface acidity of the synthesized materials. After pyridine adsorption at 40 °C, vibrational bands corresponding to pyridine species were observed in the 1400–1650 cm^{-1} region; the obtained spectra are shown in Fig. 4a. Pyridine adsorbed 1Pd@Al_2O_3 catalyst exhibits acidic bands. The band at around 1445 cm^{-1} corresponds to strong Lewis acid sites and the band at 1490 cm^{-1} corresponds to the adsorption of pyridinium ions on both Lewis and Brønsted acid sites. 1610 cm^{-1} and 1575 cm^{-1} bands were assigned to the strong and weak Lewis acid sites, respectively, while the band at 1593 cm^{-1} was attributed to the hydrogen-bound pyridine. Brønsted acid sites that show bands at 1540 cm^{-1} and 1640 cm^{-1} were not observed in the catalysts [54, 76–79]. As expected, the alumina-supported catalyst had acidic sites, and these acidic sites were eliminated from the catalyst structure with the addition of CaO.

CO_2-TPD analysis was conducted to determine the distribution of basic sites on the reduced catalysts. According to the studies, materials may show three types of CO_2 desorption peaks, which are attributable to weak, moderate, and strong basic sites [54]. CO_2 is adsorbed linearly (O═C═O─M) on weakly basic sites, forming a bridge-type configuration ($_{(C<^{O-M}_{O-M})}$) on moderate and strong basic sites. This bridging configuration was formed by the adsorption of each oxygen in the CO_2 to the metal catalyst surface; this makes it more difficult to remove the adsorbed CO_2. As a result, the desorption temperature increases to 350–550 ºC in moderately basic adsorption sites and to 600 ºC in case of removal from strong basic sites [80]. The CO_2-TPD profile of Al_2O_3 showed a strong CO_2 desorption peak around 130 °C attributed to the weak basic site and a weak peak around 540 °C attributed to the moderate basic site (Fig. 4b). With the addition of Pd to alumina, there was a significant decrease in the weak basic site peak intensity, while the peak in the moderate basic site shifted to the strong basic site and increased in intensity as well. The CO_2-TPD profile of

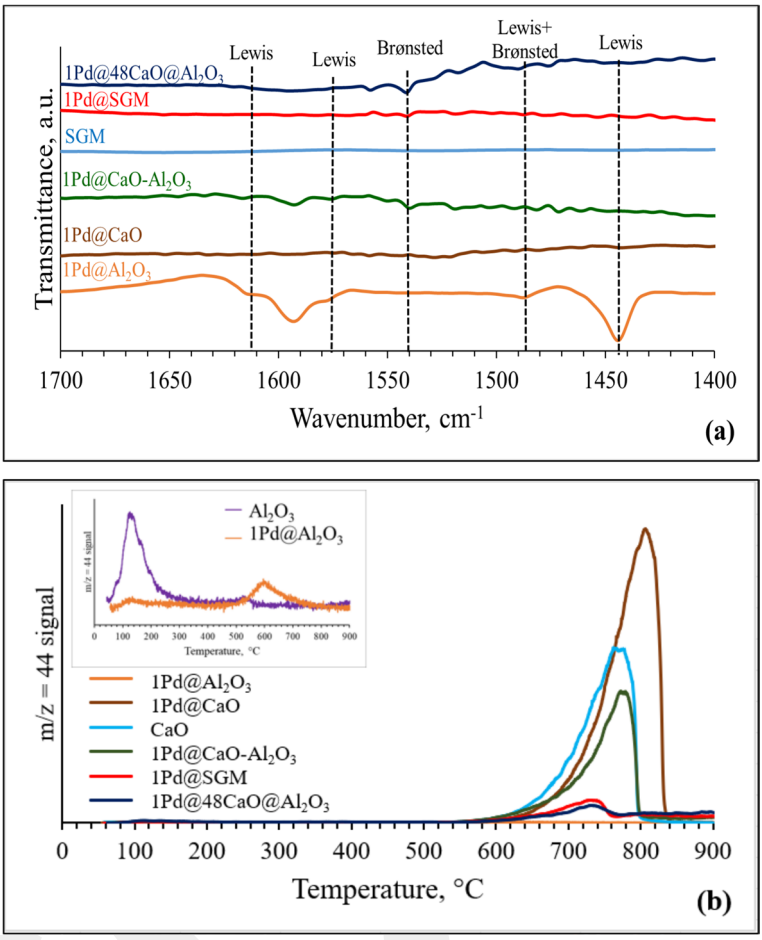

Fig. 4 (**a**) DRIFTS spectra of the reduced catalysts after pyridine adsorption at 40 °C and (**b**) CO_2-TPD analysis of the reduced catalysts

CaO showed a CO_2 desorption peak in the strong basic site at ~ 760 ºC. The addition of Pd to the CaO material increased the peak intensity of the strong basic site. 1Pd@CaO catalyst shows a high-intensity peak for strong basic sites at 808 ºC. As expected, the addition of CaO to the Al_2O_3 support material increased the density of basic sites. Strong basic sites were obtained at approximately 778 ºC, 738 ºC, and 739 ºC in 1Pd@CaO–Al_2O_3, 1Pd@SGM, and 1Pd@48CaO@Al_2O_3 catalysts, respectively. These results are in agreement with the pyridine DRIFTS analysis.

XPS analyses were performed to determine the nature of the Pd compound in the synthesized materials. Complete spectra of O 1s, C 1s, Al 2p, Ca 2p, and Pd 3d regions were collected for each catalyst sample. Charge shifting was adjusted for in the data using C 1s binding energy of 284.5 eV. XPS spectra of the reduced catalysts Pd 3d region are given in Fig. 5. The Ca 2p region (342–354 eV) [81]

and the Pd 3d (330–346 eV) [82] regions for different catalysts show almost identical behavior. The low Pd ratio in the catalysts and the overlap with the Ca region caused the peak intensities to be low. Since the Pd peak intensities of the Ca-free 1Pd@Al_2O_3 catalyst were obtained relatively better than the other catalysts, the Pd 3d region of this catalyst is given separately (Fig. 5a). 1Pd@Al_2O_3 catalysts showed two strong peaks at binding energies of around 336 and 341 eV that were assigned to the Pd $3d_{5/2}$ and Pd $3d_{3/2}$. The peaks obtained indicate the presence of metallic palladium (Pd^0 species) in the structure, as expected [22, 83–85]. The Pd 3d regions of the synthesized Ca-containing catalysts are given in Fig. 5b. The two peaks seen between 340.5–341 and 335–336 eV in the XPS spectra of all catalysts belong to metallic palladium similar to the 1Pd@Al_2O_3 catalyst. These results show that the reduction process was carried out successfully, and all palladium crystals on the catalysts synthesized are in the reduced state.

SEM analysis was used to determine the surface morphology of the synthesized catalysts and metal distributions. SEM images of the synthesized catalysts are given

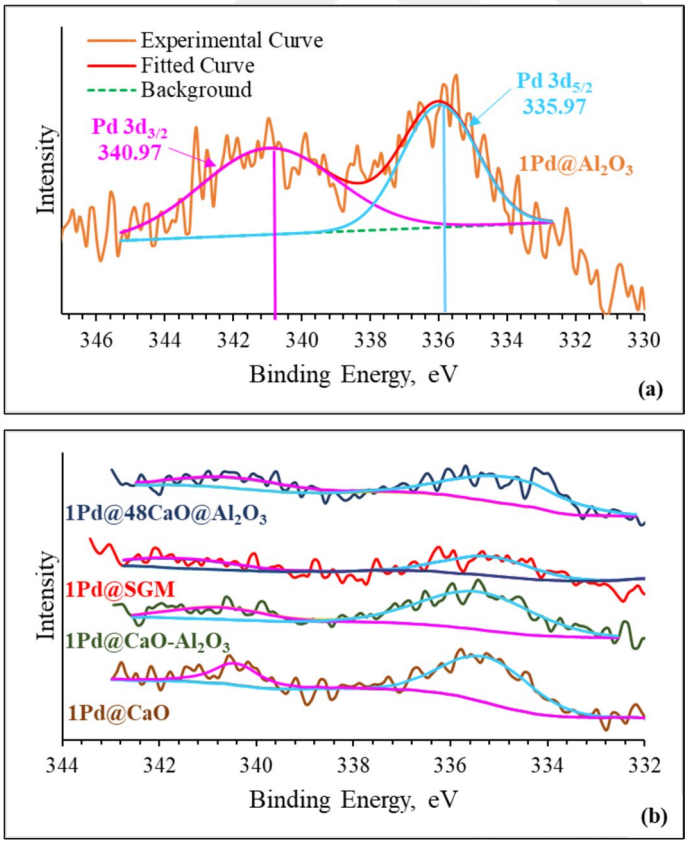

Fig. 5 XPS spectra of Pd 3d region for the reduced (**a**) 1Pd@Al_2O_3 catalyst and (**b**) 1Pd@CaO, 1Pd@CaO–Al_2O_3, 1Pd@SGM, 1Pd@48CaO@Al_2O_3 catalysts

in Fig. 6. Alumina, calcium oxide, and mayenite supported monometallic catalysts showed various structures with different morphologies resulting from the combination of different species. In alumina-supported materials, slit-like wall structures are observed. Only the material with CaO support (1Pd@CaO) shows calcium oxide's spongy and foamed spherical structure. Elemental mapping of Al, Ca, and Pd carried out for 1Pd@SGM and 1Pd@48CaO@Al_2O_3 catalysts showed a well-dispersion of palladium within the structures (Fig. 7). The chemical composition of the synthesized materials and the concentrations of palladium contained in them were determined using the energy-dispersive X-ray spectroscopy (EDS) technique together with the SEM technique. EDS results given in Table 2 showed that the percentage of Pd metal on the catalyst surface was in line with the desired loading ratios within the

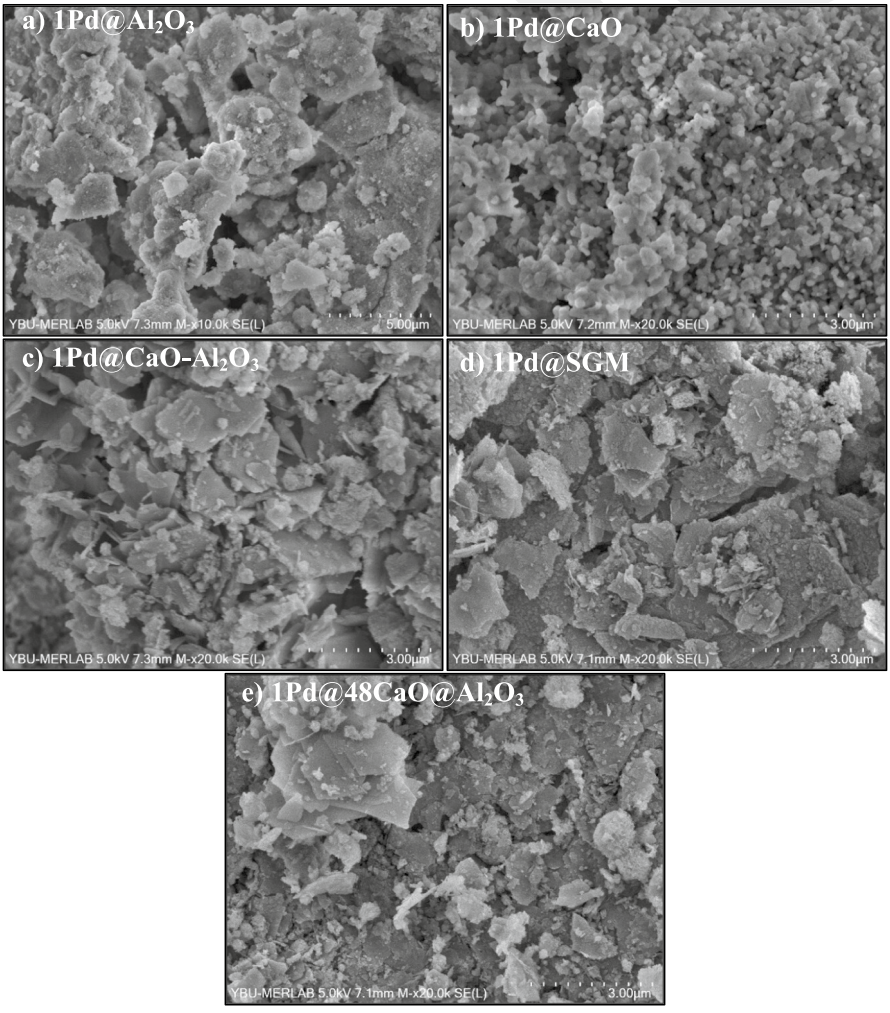

Fig. 6 SEM images of the reduced catalysts

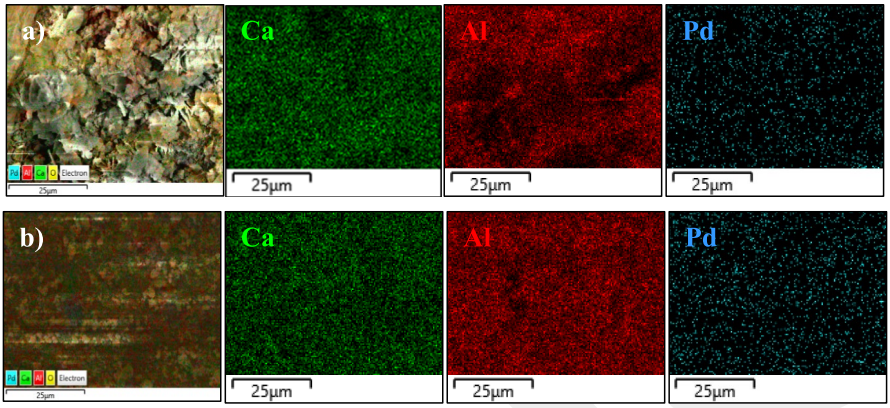

Fig. 7 SEM–EDX images of the reduced (**a**) 1Pd@SGM and (**b**) 1Pd@48CaO@Al_2O_3 catalysts

catalyst structure, which suggests that the active metal was distributed evenly within the structure. While EDS analysis focuses primarily on specific surface morphology in elemental analysis, ICP-OES analysis can accurately detect the metal composition of the complete sample. Therefore, the palladium contents of the synthesized catalysts were also determined by ICP-OES analysis (Table 2). As a result of the analysis, it was determined that the palladium percentages were close to the desired ratios and that it was successfully impregnated onto the support materials.

Activity test results

Methanol decomposition reactions were carried out in the 100–400 ºC temperature range for 6 h. The methanol decomposition reaction is endothermic, and according to Le Chatelier's principle, as the temperature increases, the equilibrium shifts in the direction of the products. However, while the methanol decomposition reaction takes place, by-products such as dimethyl ether, methane, and carbon dioxide can also be formed depending on the temperature and the structural and physical properties of the catalyst used. For this reason, most of the test studies carried out were conducted in the form of temperature scanning in the literature. Since catalysts with different structural and physical properties were used in this study, the range of 100–400 °C was decided by considering the literature studies to examine the temperature effect. The duration of the temperature scan was determined by considering the equilibrium state of the system for each temperature. The performances of the synthesized catalysts were evaluated in terms of methanol conversion and selectivity of H_2, CO, CO_2, CH_4, C_2H_6O, CH_2O_2, and CH_2O. All catalysts showed catalytic activity above 200 ºC (Fig. 8a). 1Pd@Al_2O_3 catalyst showed higher methanol conversion compared to the 1Pd@CaO catalyst at all reaction temperatures. However, when evaluated in terms of product selectivity (Fig. 8b, c and d), the 1Pd@Al_2O_3 catalyst predominantly catalyzed the methanol dehydration reaction ($2CH_3OH \leftrightarrow CH_3OCH_3 + H_2O$) and produced DME. This result is not surprising since the DRIFTS analysis showed

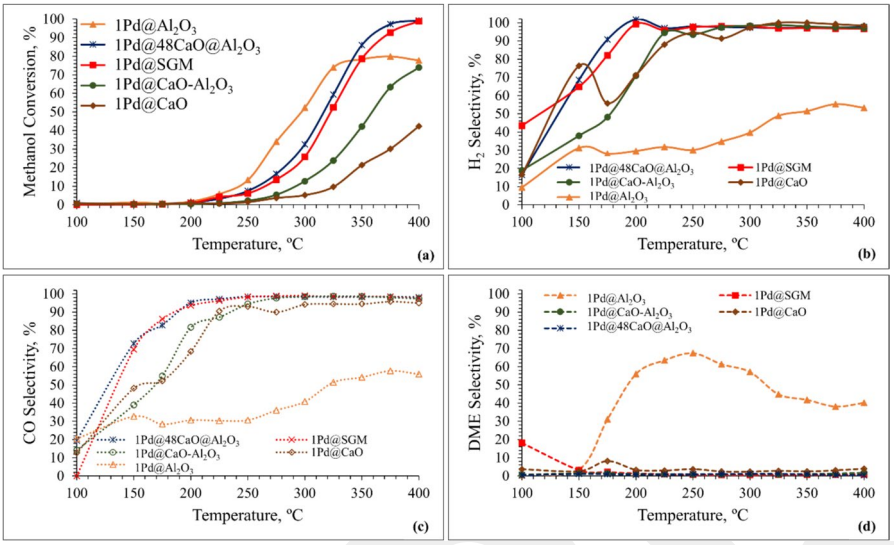

Fig. 8 Catalytic activity test results of the synthesized reduced catalysts at different temperatures (**a**) methanol conversion, (**b**) hydrogen selectivity, (**c**) carbon monoxide selectivity, and (**d**) dimethyl ether selectivity (GHSV: 21,600 ml/h.g_{cat}, Methanol/Argon: 1/5)

the presence of surface acidity on this catalyst and acidic catalysts favor the ether formation. In the 1Pd@CaO catalyst that has no surface acidity, it was determined that DME selectivity was below 5% and methanol decomposition was the main reaction. 1Pd@CaO catalyst produced H_2 and CO as desired, but methanol conversion was limited on this catalyst. To increase the conversion by keeping the H_2 and CO selectivity high, alumina and CaO were physically mixed in equal proportions to obtain the support material, with the aim of reducing alumina's acidity by using calcium, an alkaline element. Higher methanol conversion was obtained at all temperatures with the 1Pd@CaO–Al_2O_3 catalyst compared to the 1Pd@CaO catalyst. In addition, while DME selectivity is high in the 1Pd@Al_2O_3 catalyst, with the addition of calcium oxide, DME selectivity is reduced below 2% and the main products are H_2 and CO in the 1Pd@CaO–Al_2O_3 catalyst, as expected. 1Pd@CaO–Al_2O_3 catalyst exhibited lower methanol conversion than the 1Pd@Al_2O_3 catalyst, which may be due to the decrease in surface area with the addition of CaO (Table 2). In addition, it was determined that $CaCO_3$ and $Ca(OH)_2$ phases were present in the XRD patterns of CaO-supported catalysts (Fig. 2b). As important as the active metal used in catalytic activity test studies, the support's structural and physical properties also significantly affect performance. A study performed with the methanol decomposition reaction in the presence of CaO support has not been reported, but in other studies, such as biodiesel production [86], it has been reported that $CaCO_3$ formed in the presence of CaO reduces the effectiveness of the catalyst. At 400 ºC, both catalysts showed approximately the same methanol conversion, and the DME selectivity of 1Pd@Al_2O_3 and 1Pd@CaO–Al_2O_3 catalysts were 40.12% and 1.64%, respectively. In

the presence of 1Pd@Al_2O_3, 1Pd@CaO, and 1Pd@CaO–Al_2O_3 catalysts, CH_4, CO_2, CH_2O_2, and CH_2O by-products with selectivities of less than 5% were also observed.

As expected, adding CaO to Al_2O_3 increased the H_2 and CO selectivity and higher methanol conversion was achieved compared to the 1Pd@CaO catalyst. Mayenite ($12CaO.7Al_2O_3$), which has a unique crystal structure containing CaO and Al_2O_3, was also used as a support material, and its activity in the methanol decomposition reaction was tested. In the presence of mayenite-supported palladium catalyst (1Pd@SGM), higher methanol conversion than 1Pd@CaO and 1Pd@CaO–Al_2O_3 catalysts was achieved at all temperatures. The main products observed with this catalyst are H_2 and CO, and the selectivity of DME is calculated below 1% at 250 ºC and above. The selectivities of the other by-products (CH_4, CO_2, CH_2O) obtained in the 1Pd@SGM catalyst are also below 1%. At 350 ºC, 1Pd@SGM and 1Pd@Al_2O_3 catalysts show approximately the same methanol conversions (78%), while DME selectivities are 0.64% and 41.79%, respectively. Above 350 ºC, 1Pd@SGM catalyst showed higher activity compared to the 1Pd@Al_2O_3, 1Pd@CaO, and 1Pd@CaO–Al_2O_3 catalysts and gave almost complete conversion (99%) at 400 ºC. The synthesized 1Pd@SGM catalyst has no surface acidity (Fig. 4a) and has strong basic sites (Fig. 4b). The structural properties of the support directly affect the product selectivity in the methanol decomposition. It was mentioned that $CaCO_3$ phase is formed in the presence of CaO support, and this may negatively affect catalytic activity. This is a difficulty encountered in processes using CaO and is considered a problem that needs to be overcome. This study shows that catalytic activity increases with the addition of CaO to acidic Al_2O_3 material, and that mayenite, which is a unique structure of calcium and aluminum oxide, exhibits high activity with its synergistic effect. While no $CaCO_3$ phase is observed in the XRD analysis of 1Pd@SGM (Fig. 2a), its presence in FTIR analysis (Fig. 2c) shows that it contains a small amount of $CaCO_3$ compared to CaO-supported materials. At this point, the importance of using mayenite as a support material in the methanol decomposition reaction becomes apparent.

To demonstrate the effect of calcium oxide on methanol decomposition and compare with the synthesized mayenite support, 48 wt% CaO, which represents the same Ca/Al ratio as the structure of mayenite, was added to the Al_2O_3 by the impregnation method. 1Pd@48CaO@Al_2O_3 catalyst showed catalytic activity close to the 1Pd@SGM catalyst in methanol decomposition. The methanol conversions and product selectivities obtained in the presence of these two catalysts are quite similar. As a result of the characterization studies, it was observed that the crystal structure, surface area, acidic, and basic properties of the 1Pd@48CaO@Al_2O_3 catalyst were also very similar to the 1Pd@SGM catalyst. The fact that the structural and physical properties of the catalysts are similar explains the almost identical catalytic activity obtained from both catalysts.

The H_2/CO ratio was calculated for catalytic activity tests at different temperatures, and it was determined that the H_2/CO ratio was between 1.91 and 2 above 250 °C for all catalysts except the 1Pd@CaO catalyst. It was found that the H_2/CO ratio exceeded 2 in the temperature range of 300–375 °C in the 1Pd@CaO catalyst and reached a maximum of 2.17 at 325 °C. These ratios are around the optimum H_2/

CO ratio for Fischer–Tropsch process for the production of liquid synthetic fuels [87].

To investigate the catalytic stabilities of 1Pd@SGM, 1Pd@Al_2O_3, and 1Pd@48CaO@Al_2O_3 catalysts, methanol decomposition reaction was carried out at 350 ºC for 6 h using spent catalysts in the temperature scan. The reaction temperature was chosen as 350 ºC since the catalysts showed close methanol conversion according to the temperature scan results at this temperature. Methanol conversion and product selectivity graphs obtained as a result of time on-stream studies are given in Figs. 9a and b, respectively. It has been determined that the catalysts remain stable for 6 h and the main products with the use of 1Pd@SGM and 1Pd@48CaO@Al_2O_3 catalysts are H_2 and CO. On the other hand, it was observed that the main

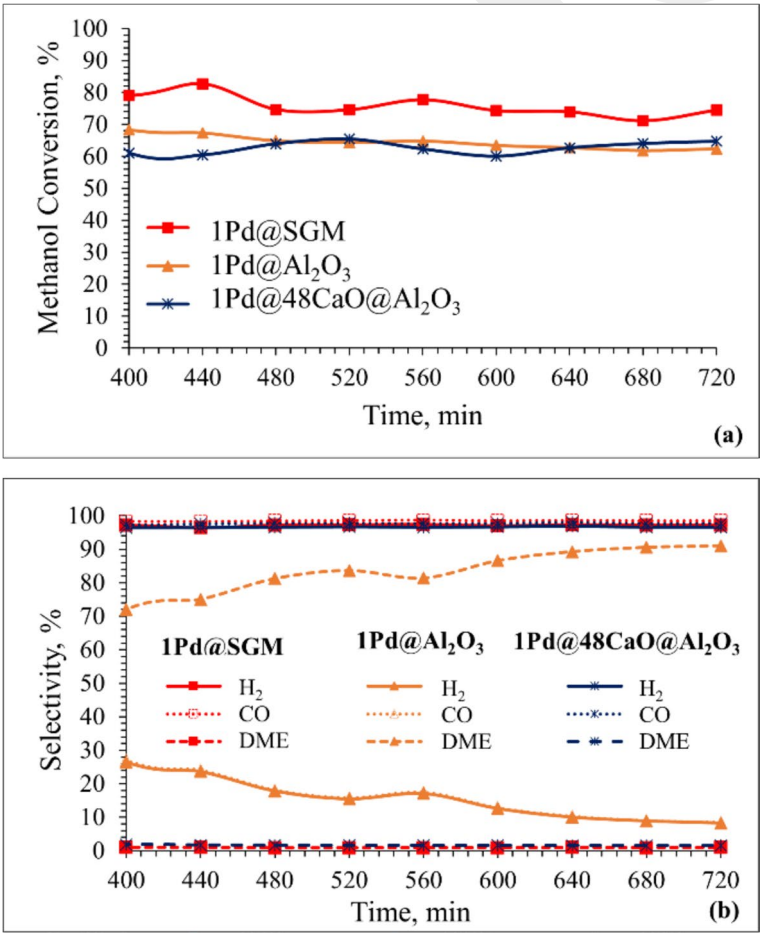

Fig. 9 (**a**) Methanol conversion, (**b**) hydrogen, carbon monoxide, and dimethyl ether selectivity over the spent 1Pd@SGM,1Pd@Al_2O_3, and 1Pd@48CaO@Al_2O_3 catalysts at 350 ºC (GHSV: 21,600 ml/h.g_{cat}, Methanol/Argon: 1/5)

product of the 1Pd@Al_2O_3 catalyst was DME and while the H_2 and CO selectivity with the use of this catalyst decreased over time, the DME selectivity increased. The average DME selectivities obtained for 350 ºC temperature after 12 h of reaction are 0.9%, 1.6%, and 79.2% for 1Pd@SGM, 1Pd@48CaO@Al_2O_3, and 1Pd@Al_2O_3 catalysts, respectively (Table 3). The by-product (CO_2, CH_4, and CH_2O) average selectivities obtained for the three catalysts are less than 1%. Average methanol conversions obtained under the same conditions are 76.1%, 65%, and 65.8% for 1Pd@SGM, 1Pd@48CaO@Al_2O_3, and 1Pd@Al_2O_3 catalysts, respectively. Although temperature scan studies showed similar conversion and selectivity results for 1Pd@SGM and 1Pd@48CaO@Al_2O_3 catalysts, 1Pd@SGM showed slightly higher conversion during the stability test.

Characterization of the spent catalysts

Raman analyses were performed on the spent catalysts to obtain information about the carbon deposited on the catalysts during activity tests. Coke formation on the catalyst surface occurs as a result of the Boudouard reaction (Eq. 16) and methane cracking (Eq. 17). Methane cracking is most effective at temperatures over 550–600 ºC, depending on the catalyst type and composition. However, because of its exothermic nature, the Boudouard reaction has favorable thermodynamics at low temperatures [1, 88]. Therefore, in the temperature range of the methanol decomposition reaction, the Boudouard reaction is expected to be effective in carbon deposition.

$$2CO \leftrightarrow C + CO_2 \ \Delta H^{\circ}_{298} = -173 \text{ kJ mol}^{-1} \tag{16}$$

$$CH_4 \rightarrow C + 2H_2 \ \Delta H^{\circ}_{298} = 75 \text{ kJ mol}^{-1} \tag{17}$$

Post-reaction characterizations were applied on used 1Pd@Al_2O_3, 1Pd@SGM, and 1Pd@48CaO@Al_2O_3 catalysts after stability testing at 350 ºC. In Fig. 10, the Raman spectrum obtained for the spent catalysts is shown for the carbon region. For carbon-containing materials, the strongest Raman bands are the D band (1300 ~ 1400 cm^{-1}), G band (~ 1580 cm^{-1}), and 2D band (2600 ~ 2700 cm^{-1}) [89–91]. No carbon bands were observed in the Raman spectra of the spent catalysts indicating no coking on the samples.

Table 3 Catalytic activity test results over the reduced 1Pd@SGM, 1Pd@Al_2O_3, and 1Pd@48CaO@Al_2O_3 catalysts at 350 ºC (GHSV:21,600 ml/h.g_{cat}, Methanol/Argon: 1/5)*

Catalysts	Methanol conversion, %	H_2/CO ratio	Selectivity, %						
			H_2	CO	DME	CH_4	CO_2	CH_2O_2	CH_2O
1Pd@SGM	76.1	1.97	97.1	98.5	0.9	0.16	0.3	0	0.15
1Pd@Al_2O_3	65.8	1.97	19.1	19.7	79.2	0.89	0	0	0.19
1Pd@48CaO@Al_2O_3	65.0	1.97	96.6	97.8	1.6	0.13	0.4	0	0.12

*Average data after 12 h

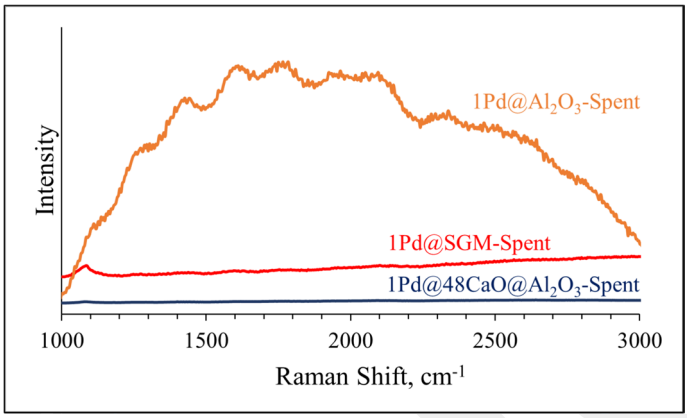

Fig. 10 Raman spectra of the spent 1Pd@Al_2O_3, 1Pd@SGM, and 1Pd@48CaO@Al_2O_3 catalysts

In addition to the Raman analysis, XRD analyses of the spent catalysts were performed to determine possible changes in the crystal structure of the catalyst during methanol decomposition reaction tests (Fig. 11). In the XRD patterns of the spent 1Pd@SGM and 1Pd@Al_2O_3 catalysts, no different phase was found compared to fresh catalysts (Fig. 2a). In the spent 1Pd@48CaO@Al_2O_3 catalyst, the $CaAl_2O_4$ phase appeared, which was not present in the fresh catalyst. This phase, which is also seen in the 48CaO@Al_2O_3 before Pd impregnation, was re-formed under the reaction conditions. XRD analysis results showed that fresh 1Pd@SGM and 1Pd@48CaO@Al_2O_3 catalysts have the same crystal structure (Fig. 2a). The fact that there is no change in the crystal structure of the 1Pd@SGM catalyst after the reaction reveals that its structure is more stable compared to the 1Pd@48CaO@Al_2O_3 catalyst. In XRD analysis, the characteristic peak of carbon appears at 2θ: 26.2° [52]. The absence of this peak in spent catalysts indicates that carbon is not formed in the structure, which confirms the results of Raman analysis (Fig. 10).

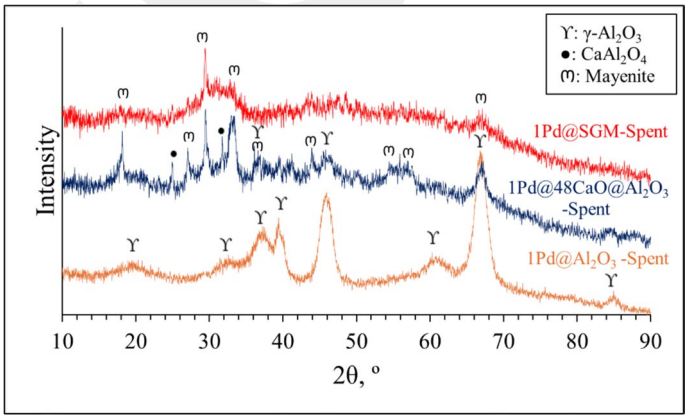

Fig. 11 XRD pattern of the spent 1Pd@SGM, 1Pd@48CaO@Al_2O_3, and 1Pd@Al_2O_3 catalysts

Conclusions

Methanol decomposition was carried out over Pd-containing alumina and/or calcium oxide-supported catalysts. The effect of CaO incorporation to alumina on the reaction was evaluated in terms of methanol conversion and product selectivity. Characterization results revealed that CaO addition decreased the surface acidity of alumina and intensified basic regions. In this way, the selectivity for DME, which is one of the important by-products of methanol decomposition, decreased, while the selectivity for hydrogen and carbon monoxide, which are the main products, increased. A significant amount of DME was produced in the presence of $1Pd@Al_2O_3$ catalyst, while trace amounts of DME were observed in catalysts containing CaO. Stability testing was also carried out using 1Pd@SGM, $1Pd@Al_2O_3$, and $1Pd@48CaO@Al_2O_3$ catalysts, which showed higher methanol conversion as a result of the temperature scan. These catalysts used in the temperature scanning activity studies that last for 6 h also showed stable activity for 6 h at 350 °C during stability testing. As a result of a total of 12 h of activity test studies, DME selectivity was determined to be below 2% in catalysts containing CaO, while it was found to be 79.2% for the $1Pd@Al_2O_3$ catalyst. With the addition of CaO to the structure, the surface acidity of alumina was removed and DME produced by methanol dehydration was reduced, increasing hydrogen and carbon monoxide selectivity. In conclusion, 1Pd@SGM and $1Pd@48CaO@Al_2O_3$ catalysts showed higher methanol conversion than other catalysts above 350 °C reaching almost 100% at 400 °C and higher hydrogen and carbon monoxide selectivity at all temperatures compared to the $1Pd@Al_2O_3$ catalyst, and the 1Pd@SGM catalyst displayed slightly higher activity than the $1Pd@48CaO@Al_2O_3$ catalyst during the stability tests. In addition, the $CaCO_3$ phase, which occurs in the presence of CaO-supported catalysts and may adversely affect catalytic activity, has been less detected in the presence of mayenite support. This study reveals that catalytic activity increases with the addition of CaO to acidic Al_2O_3, and that mayenite, which is a calcium and aluminum oxide with a unique structure, shows the best activity with its synergistic effect.

Acknowledgements This work was supported by the Scientific and Technological Research Council of Türkiye (TUBITAK) BIDEB-2232 Program (118C237), Gazi University Research Fund (FDK-2023-8907), TUBITAK-2211 PhD Scholarship Program, and TUBITAK-2250 Performance-Based Scholarships Program for PhD. The authors thank the Central Laboratory of METU, Central Laboratory of AYBU, and Atilim University Metal Forming Center of Excellence for the characterization results of the synthesized materials.

Author contributions Busra Eryildirim: Investigation, Validation, Methodology, Formal analysis, Visualization, Writing – original draft. Nuray Oktar: Investigation, Methodology, Supervision, Project administration, Writing – review & editing. Doruk Dogu: Investigation, Methodology, Supervision, Project administration, Writing – review & editing.

Funding Open access funding provided by the Scientific and Technological Research Council of Türkiye (TÜBİTAK). Türkiye Bilimsel ve Teknolojik Araştırma Kurumu (TUBITAK), 118C237, Gazi Üniversitesi, FDK-2023-8907.

Data availability No datasets were generated or analysed during the current study.

Declarations

Conflict of interest The authors declare no competing interests.

References

1. N.C. Sahingoz, K. Talu, N. Oktar, T. Dogu, I. Pamuk, On-site hydrogen-rich gas production from diesel: a comprehensive study on catalyst development with nickel and diverse metal oxides (MgO, La_2O_3, CeO_2, SiO_2) supported on alumina. Appl. Catal. A Gen. **687**, 119940 (2024)
2. D. Dogu, H. Sohn, S. Bhattacharya, C. Cornelius, U.S. Ozkan, Using volatile organic compounds in waste streams as fuel. Int. J. Chem. React. Eng. **17**, 1 (2019)
3. B.P. Karaman, E.K. Ekinci, Non-oxidative ethane dehydrogenation reaction over molybdenum and chromium incorporated MgO encapsulated carbon-core catalysts in microwave reactor. Res. Chem. Intermed. **50**, 3197 (2024)
4. B. Mahant, P. Linga, R. Kumar, Hydrogen economy and role of hythane as a bridging solution: A perspective review. Energy Fuels **35**, 15424 (2021)
5. Y.H. Zhao, H.X. Luo, X.Q. Feng, Q.J. Zhang, H. Wang, J.K. Zhang, Enhancement of catalytic activity over Cu-supported montmorillonite catalyst for hydrogen production via steam reforming of dimethyl ether. Res. Chem. Intermed. **50**, 669 (2024)
6. G. Li, C. Gu, W. Zhu, X. Wang, X. Yuan, Z. Cui, H. Wang, Z. Gao, Hydrogen production from methanol decomposition using Cu-Al spinel catalysts. J. Clean. Prod. **183**, 415 (2018)
7. S.S. Mabaleha, P. Kalita, Enhancing hydrogen production in methanol steam reforming using PdZn-based catalysts: a mini-review on CO suppression. Energy Fuels **38**, 13565 (2024)
8. B. Eryildirim, H. Arbag, N. Oktar, G. Dogu, Comparison of microwave and conventionally heated reactor performances in catalytic dehydrogenation of ethane. Int. J. Hydrogen Energy **46**, 5296 (2021)
9. J. Zhao, R. Shi, Z. Li, C. Zhou, T. Zhang, How to make use of methanol in green catalytic hydrogen production? Nano Sel. **1**, 12 (2020)
10. I. Orozco, E. Huang, M. Mahapatra, R. Shi, J. Kang, S. Nemšák, S.D. Senanayake, P. Liu, J.A. Rodriguez, In situ studies of methanol decomposition over Cu(111) and Cu_2O/Cu(111): effects of reactant pressure, surface morphology, and hot spots of active sites. J. Phys. Chem. C **125**, 558 (2021)
11. J. Xi, Z. Wang, G. Lu, Improvement of Cu/Zn-based catalysts by nickel additive in methanol decomposition. Appl. Catal. A Gen. **225**, 77 (2002)
12. Y. Wei, S. Li, J. Jing, M. Yang, C. Jiang, W. Chu, Synthesis of Cu–Co catalysts for methanol decomposition to hydrogen production via deposition–precipitation with urea method. Catal. Lett. **149**, 2671 (2019)
13. J.Y. Damte, S.L. Lyu, E.G. Leggesse, J.C. Jiang, Methanol decomposition reactions over a boron-doped graphene supported Ru-Pt catalyst. Phys. Chem. Chem. Phys. **20**, 9355 (2018)
14. D.G. Araiza, A. Gómez-Cortés, G. Díaz, Reactivity of methanol over copper supported on well-shaped CeO_2: a TPD-DRIFTS study. Catal. Sci. Technol. **7**, 5224 (2017)
15. P.H. Matter, D.J. Braden, U.S. Ozkan, Steam reforming of methanol to H_2 over nonreduced Zr-containing CuO/ZnO catalysts. J. Catal. **223**, 340 (2004)
16. Y. Xu, H. Jin, J. Zhang, Y. Matsushita, Carbon deposition–resistant Ni_3Sn nanoparticles with highly stable catalytic activity for methanol decomposition. Appl. Catal. A Gen. **608**, 117872 (2020)

17. J. Jing, L. Li, W. Chu, Y. Wei, C. Jiang, Microwave-assisted synthesis of high performance copper-based catalysts for hydrogen production from methanol decomposition. Int. J. Hydrogen Energy **43**, 12059 (2018)
18. M. Tommasi, D. Ceriotti, A. Gramegna, S.N. Degerli, G. Ramis, I. Rossetti, Oxidative steam reforming of methanol over Cu-based catalysts. Catalysts **14**, 759 (2024)
19. Z. Sun, X. Zhang, H. Li, T. Liu, S. Sang, S. Chen, L. Duan, L. Zeng, W. Xiang, J. Gong, Chemical looping oxidative steam reforming of methanol: A new pathway for auto-thermal conversion. Appl. Catal. B Environ. **269**, 118758 (2020)
20. R. Ben David, A. Ben Yaacov, A.R. Head, B. Eren, Methanol decomposition on copper surfaces under ambient conditions: mechanism, surface kinetics, and structure sensitivity. ACS Catal. **12**, 7709 (2022)
21. P.H. Matter, U.S. Ozkan, Effect of pretreatment conditions on Cu/Zn/Zr-based catalysts for the steam reforming of methanol to H_2. J. Catal. **234**, 463 (2005)
22. F. Cai, Y. Guo, J.J. Ibrahim, J. Zhang, Y. Sun, A highly active and stable Pd/MoC catalyst for hydrogen production from methanol decomposition. Appl. Catal. B Environ. **299**, 120648 (2021)
23. H. Borchert, B. Jürgens, T. Nowitzki, P. Behrend, Y. Borchert, V. Zielasek, S. Giorgio, C.R. Henry, M. Bäumer, Decomposition of methanol by Pd Co, and bimetallic Co-Pd catalysts: a combined study of well-defined systems under ambient and UHV conditions. J. Catal. **256**, 24 (2008)
24. S.T. Yong, K. Hidajat, S. Kawi, The roles of Cu, Zn and Mn in $Cu_{0.5}Zn_{0.5}Mn_2O_4$ spinel-lattice catalyst for methanol decomposition. Catal. Today **131**, 188–196 (2008)
25. S. Qing, X. Hou, L. Li, G. Feng, X. Wang, Z. Gao, W. Fan, Deactivation feature of Cu/SiO_2 catalyst in methanol decomposition. Int. J. Hydrogen Energy **44**, 16667 (2019)
26. T. Tsoncheva, C. Rosmini, M. Mihaylov, J. Henych, K. Chakarova, N. Velinov, D. Kovacheva, Z. Němečková, M. Kormunda, R. Ivanova, I. Spassova, K. Hadjiivanov, Nickel-decorated mesoporous iron-cerium mixed oxides: microstructure and catalytic activity in methanol decomposition. ACS Appl. Mater. Interfaces **14**, 873 (2022)
27. M. Mihaylov, T. Tsoncheva, K. Hadjiivanov, Structure sensitivity of methanol decomposition on Ni/SiO_2 catalysts. J. Mater. Sci. **46**, 7144 (2011)
28. Y. Matsumura, N. Tode, T. Yazawa, M. Haruta, Catalytic methanol decomposition to carbon monoxide and hydrogen over Ni SiO_2 of high nickel content. J. Mol. Catal. A. Chem. **99**, 183 (1995)
29. H. Mitani, Y. Xu, T. Hirano, M. Demura, R. Tamura, Catalytic properties of Ni-Fe-Mg alloy nanoparticle catalysts for methanol decomposition. Catal. Today **281**, 669 (2017)
30. L. López-Rodríguez, D.G. Araiza, D.G. Arcos, A. Gómez-Cortés, G. Díaz, Bimetallic Cu-Pt catalysts over nanoshaped ceria for hydrogen production via methanol decomposition. Catal. Today **394–396**, 486 (2022)
31. J.C. Brown, E. Gulari, Hydrogen production from methanol decomposition over Pt/Al_2O_3 and ceria promoted Pt/Al_2O_3 catalysts. Catal. Commun. **5**, 431 (2004)
32. A.V. Miller, V.V. Kaichev, I.P. Prosvirin, V.I. Bukhtiyarov, Mechanistic study of methanol decomposition and oxidation on Pt(111). J. Phys. Chem. C **117**, 8189 (2013)
33. Q. Zhang, G. Liu, L. Wang, X. Zhang, G. Li, Controllable decomposition of methanol for active fuel cooling technology. Energy Fuels **28**, 4431 (2014)
34. P. Du, P. Wu, C. Cai, Mechanism of methanol decomposition on the $Pt_3Ni(111)$ surface: DFT study. J. Phys. Chem. C **121**, 9348 (2017)
35. F. Carraro, A. Fapohunda, M.C. Paganini, S. Agnoli, Morphology and size effect of ceria nanostructures on the catalytic performances of Pd/CeO_2 catalysts for methanol decomposition to syngas. ACS Appl. Nano Mater. **1**, 1492 (2018)
36. L.A. Luque-Álvarez, A. Núñez-Carballo, B. Lacroix, R. Sánchez-de-Armas, M.A. Centeno, L. Pastor-Pérez, L.F. Bobadilla, J.A. Odriozola, Exploring the impact of nanoshaped ceria in the methanol decomposition reaction pathway for clean energy production. Appl. Catal. B Environ. **361**, 124649 (2025)
37. M. Zhao, H. Zhang, X. Li, Y. Chen, Co-modified Pd/CeO_2-ZrO_2 catalysts for methanol decomposition. J. Energy Chem. **23**, 755 (2014)
38. S. Hokenek, J.N. Kuhn, Methanol decomposition over palladium particles supported on silica: role of particle size and co-feeding carbon dioxide on the catalytic properties. ACS Catal. **2**, 1013 (2012)
39. D.G. Araiza, A. Gómez-Cortés, G. Díaz, Methanol decomposition over bimetallic Cu-M catalysts supported on nanoceria: effect of the second metal on the catalytic properties. Catal. Today **356**, 440 (2020)

40. T. Shishido, H. Sameshima, T. Hayakawa, S. Hamakawa, E. Tanabe, K. Ito, K. Takehira, Methanol decomposition to synthesis gas over supported Pd catalysts prepared from synthetic anionic clays. Stud. Surf. Sci. Catal. **130**, 2117 (2000)
41. S. Xie, X. Zhang, P. Xu, B. Hatcher, Y. Liu, L. Ma, S.N. Ehrlich, S. Hong, F. Liu, Effect of surface acidity modulation on Pt/Al_2O_3 single atom catalyst for carbon monoxide oxidation and methanol decomposition. Catal. Today **402**, 149 (2022)
42. T. Tsoncheva, I. Genova, M. Dimitrov, E. Sarcadi-Priboczki, A.M. Venezia, D. Kovacheva, N. Scotti, V. dal Santo, Nanostructured copper-zirconia composites as catalysts for methanol decomposition. Appl. Catal. B Environ. **165**, 599 (2015)
43. M.P. Kapoor, Y. Ichihashi, K. Kuraoka, Y. Matsumura, Catalytic methanol decomposition over palladium deposited on thermally stable mesoporous titanium oxide. J. Mol. Catal. A Chem. **198**, 303 (2003)
44. J. Torres-Liñán, M. García-Rollán, J.M. Rosas, J. Rodríguez-Mirasol, T. Cordero, Deactivation of a biomass-derived zirconium-doped phosphorus-containing carbon catalyst in the production of dimethyl ether from methanol dehydration. Energy Fuels **35**, 17225 (2021)
45. M.C. Ozcan, B.P. Karaman, N. Oktar, T. Dogu, Dimethyl ether from syngas and effect of CO_2 sorption on product distribution over a new bifunctional catalyst pair containing STA@SBA-15. Fuel **330**, 125607 (2022)
46. W.H. Cheng, C.Y. Shiau, T.H. Liu, H.L. Tung, J.F. Lu, C.C. Hsu, Promotion of Cu/Cr/Mn catalyst by alkali additives in methanol decomposition. Appl. Catal. A Gen. **170**, 215 (1998)
47. S. Yang, J.N. Kondo, K. Hayashi, M. Hirano, K. Domen, H. Hosono, Partial oxidation of methane to syngas over promoted C12A7. Appl. Catal. A Gen. **277**, 239 (2004)
48. L. Huang, Y. Ma, M. Niu, S. Ren, Q. Guo, C. Xu, B. Shen, Formation of H_2O in the CH_4-CO_2 dry reforming process and its activation to this reaction over Ni-Fe/MC12A7 catalysts. Appl. Catal. B Environ. **334**, 122822 (2023)
49. C. Manera, D. Perondi, G.L. Dotto, T. Barcellos, M. Godinho, Study of mayenite produced from waste eggshell as support for Ni–Co catalysts for biomass tar cracking. Chem. Eng. Res. Des. **176**, 218 (2021)
50. C. Dang, H. Xia, S. Yuan, X. Wei, W. Cai, Green hydrogen production from sorption-enhanced steam reforming of biogas over a Pd/Ni–CaO-mayenite multifunctional catalyst. Renew. Energy **201**, 314 (2022)
51. J.R. Salasin, S.E.A. Schwerzler, M.R. Koehler, D.J. Keffer, C.J. Rawn, The effect of process parameters on the amorphous citrate sol-gel synthesis of Cu-doped $Ca_{12}Al_{14}O_{33}$. Materialia **4**, 466 (2018)
52. H. Akansu, H. Arbag, H.M. Tasdemir, S. Yasyerli, N. Yasyerli, G. Dogu, Nickel-based alumina supported catalysts for dry reforming of biogas in the absence and the presence of H_2S: Effect of manganese incorporation. Catal. Today **397–399**, 37 (2022)
53. A. Arslan Bozdag, A.D. Deniz Kaynar, T. Dogu, N.A. Sezgi, Development of ceria and tungsten promoted nickel/alumina catalysts for steam reforming of diesel. Chem. Eng. J. **377**, 120274 (2019)
54. H. Arbag, Effect of impregnation sequence of Mg on performance of mesoporous alumina supported Ni catalyst in dry reforming of methane. Int. J. Hydrogen Energy **43**, 6561 (2018)
55. P. Krongkitsiri, W. Krongkitsiri, S. Phukird, U. Tipparach, A comparison of dielectric properties of eggshells from free-range system and control-range system. Mater. Today Proc. **47**, 3617 (2021)
56. M. Khachani, A. El Hamidi, M. Halim, S. Arsalane, Non-isothermal kinetic and thermodynamic studies of the dehydroxylation process of synthetic calcium hydroxide $Ca(OH)_2$. J. Mater. Environ. Sci. **5**, 615 (2014)
57. P.E. Sanchez-Jimenez, L.A. Perez-Maqueda, J.M. Valverde, Nanosilica supported CaO: a regenerable and mechanically hard CO_2 sorbent at Ca-looping conditions. Appl. Energy **118**, 92 (2014)
58. W. Roschat, S. Phewphong, A. Thangthong, P. Moonsin, B. Yoosuk, T. Kaewpuang, V. Promarak, Catalytic performance enhancement of CaO by hydration-dehydration process for biodiesel production at room temperature. Energy Convers. Manag. **165**, 1 (2018)
59. T. Schmid, P. Dariz, Shedding light onto the spectra of lime: Raman and luminescence bands of CaO, $Ca(OH)_2$ and $CaCO_3$. J. Raman Spectrosc. **46**, 141 (2014)
60. Z. Zhu, Y. Liu, W. Cong, X. Zhao, J. Janaun, T. Wei, Z. Fang, Soybean biodiesel production using synergistic CaO/Ag nano catalyst: process optimization, kinetic study, and economic evaluation. Ind. Crops Prod. **166**, 113479 (2021)
61. Y.P. Chang, P.H. Chang, Y.T. Lee, T.J. Lee, Y.H. Lai, S.Y. Chen, Morphological and structural evolution of mesoporous calcium aluminate nanocomposites by microwave-assisted synthesis. Microporous Mesoporous Mater. **183**, 134 (2014)

62. H. Zou, D. Peng, Z. Chu, X. Wang, Y. Li, J.-W. Hou, X. Yao, Photoluminescence and thermal stability of yellow-emitting Pr^{3+} doped $CaAl_2O_4$ phosphors. J. Adv. Dielectr. **03**, 1350022 (2013)
63. A.M. Nassar, N.F. Alotaibi, Eggshell recycling for fabrication of Pd@CaO, characterization and high-performance solar photocatalytic activity. Environ. Sci. Pollut. Res. **28**, 3515 (2021)
64. S.S. Ghazali, W.L. Kem, R. Jusoh, S. Abdullah, J.H. Shariffuddin, Evaluation of La-doped CaO derived from cockle shells for photodegradation of POME. Bull. Chem. React. Eng. Catal. **14**, 205 (2019)
65. N. Kerru, L. Gummidi, S.V.H.S. Bhaskaruni, S.N. Maddila, S.B. Jonnalagadda, One-pot green synthesis of novel 5,10-dihydro-1H-pyrazolo[1,2-b]phthalazine derivatives with eco-friendly biodegradable eggshell powder as efficacious catalyst. Res. Chem. Intermed. **46**, 3067 (2020)
66. S.E. Mahesh, A. Ramanathan, K.M.M.S. Begum, A. Narayanan, Biodiesel production from waste cooking oil using KBr impregnated CaO as catalyst. Energy Convers. Manag. **91**, 442 (2015)
67. C. Sriwong, C. Phrompet, W. Tuichai, A. Karaphun, K. Kurosaki, C. Ruttanapun, Synthesis, microstructure, multifunctional properties of mayenite $Ca_{12}Al_{14}O_{33}$ (C12A7) cement and graphene oxide (GO) composites. Sci. Rep. **10**, 1 (2020)
68. R.E. Benner, J.R. Mitchell, R.W. Grow, Raman scattering as a diagnostic technique for cathode caracterization. IEEE Trans. Electron Devices **8**, 1842 (1987)
69. A.E.A.A. Said, M.M.M. Abd El-Wahab, M. Abd El-Aal, Effect of ZrO_2 on the catalytic performance of nano γ-Al_2O_3 in dehydration of methanol to dimethyl ether at relatively low temperature. Res. Chem. Intermed. **42**, 1537 (2016)
70. S.S. Chan, I.E. Wachs, L.L. Murrell, N.C. Dispenziere, Laser Raman characterization of tungsten oxide supported on alumina: influence of calcination temperatures. J. Catal. **92**, 1 (1985)
71. D.K. Chlebda, R.J. Jedrzejczyk, P.J. Jodlowski, J. Lojewska, Surface structure of cobalt, palladium, and mixed oxide-based catalysts and their activity in methane combustion studied by means of micro-Raman spectroscopy. J. Raman Spectrosc. **48**, 1871 (2017)
72. A. Spadoni, S. Sau, N. Corsaro, M. Lanchi, A.C. Tizzoni, E. Veca, M. Falconieri, L. Della Seta, A. De Girolamo Del, L. Mauro, E. Turchetti, R.L. Mansi, Thermochemical heat storage through CaO-Mayenite/$CaCO_3$ system: Thermal performances comparison for two synthesis methods. J. Energy Storage **72**, 108386 (2023)
73. E. Dubina, L. Korat, L. Black, J. Strupi-Šuput, J. Plank, Influence of water vapour and carbon dioxide on free lime during storage at 80 °C, studied by Raman spectroscopy. Spectrochim. Acta Part A Mol. Biomol. Spectrosc. **111**, 299–303 (2013)
74. D. Torréns-Martín, L. Fernández-Carrasco, S. Martínez-Ramírez, Hydration of calcium aluminates and calcium sulfoaluminate studied by Raman spectroscopy. Cem. Concr. Res. **47**, 43 (2013)
75. J. Li, K. Chou, Q. Shu, Structure and viscosity of CaO-Al_2O_3-B_2O_3 based mould fluxes with varying CaO/Al_2O_3 mass ratios. ISIJ Int. **60**, 51 (2020)
76. G. Celik, S.A. Ailawar, S. Gunduz, P.L. Edmiston, U.S. Ozkan, Formation of carbonaceous deposits on Pd-based hydrodechlorination catalysts: vibrational spectroscopy investigations over Pd/Al_2O_3 and Pd/SOMS. Catal. Today **323**, 129 (2019)
77. C. Morterra, S. Coluccia, A. Chiorino, F. Boccuzzi, Infrared study of the adsorption of pyridine on α-Al_2O_3. J. Catal. **54**, 348 (1978)
78. X. Liu, DRIFTS study of surface of γ-alumina and its dehydroxylation. J. Phys. Chem. C **112**, 5066 (2008)
79. D. Dogu, K.E. Meyer, A. Fuller, S. Gunduz, D.J. Deka, N. Kramer, A.C. Co, U.S. Ozkan, Effect of lanthanum and chlorine doping on strontium titanates for the electrocatalytically-assisted oxidative dehydrogenation of ethane. Appl. Catal. B Environ. **227**, 90 (2018)
80. J. Wu, T. Su, Y. Jiang, X. Xie, Z. Qin, H. Ji, In situ DRIFTS study of O_3 adsorption on CaO, γ-Al_2O_3, CuO, α-Fe_2O_3 and ZnO at room temperature for the catalytic ozonation of cinnamaldehyde. Appl. Surf. Sci. **412**, 290 (2017)
81. C. Ruttanapun, P. Srepusharawoot, S. Maensiri, Effect of Fe^{3+}-doped $Ca_{12}Al_{14}O_{33}$ cement on optical and thermal properties. Chinese J. Phys. **56**, 252 (2018)
82. Z. Gohari Bajestani, A. Yürüm, Y. Yürüm, Decoration of graphene sheets with Pd/Al_2O_3 hybrid particles for hydrogen storage applications. Int. J. Hydrogen Energy **41**, 9810 (2016)
83. M. Brun, A. Berthet, J.C. Bertolini, XPS, AES and Auger parameter of Pd and PdO. J. Electron Spectros. Relat. Phenomena **104**, 55 (1999)
84. H. Peng, X. Zhang, V. Papaefthimiou, C. Pham-Huu, V. Ritleng, Pd-functionalized polydopamine-coated polyurethane foam: a readily prepared and highly reusable structured catalyst for selective alkyne semi-hydrogenation and Suzuki coupling under air. Green Chem. **25**, 264 (2022)

85. S. Yang, J. Dong, Z. Yao, C. Shen, X. Shi, Y. Tian, S. Lin, X. Zhang, One-pot synthesis of graphene-supported monodisperse pd nanoparticles as catalyst for formic acid electro-oxidation. Sci. Rep. **4**, 4501 (2014)
86. L. Macheli, M.E. Malefane, L.L. Jewell, Waste-derived calcium oxide catalysts in biodiesel production: exploring various waste sources, deactivation challenges, and improvement strategies. Bioresour. Technol. Rep. **29**, 102021 (2025)
87. D.Y. Lee, M.T. Mehran, J. Kim, S. Kim, S.B. Lee, R.H. Song, E.Y. Ko, J.E. Hong, J.Y. Huh, T.H. Lim, Scaling up syngas production with controllable H_2/CO ratio in a highly efficient, compact, and durable solid oxide coelectrolysis cell unit-bundle. Appl. Energy **257**, 114036 (2020)
88. H. Arbag, S. Yasyerli, N. Yasyerli, G. Dogu, T. Dogu, Enhancement of catalytic performance of Ni based mesoporous alumina by Co incorporation in conversion of biogas to synthesis gas. Appl. Catal. B Environ. **198**, 254 (2016)
89. Z. Li, L. Deng, I.A. Kinloch, R.J. Young, Raman spectroscopy of carbon materials and their composites: graphene, nanotubes and fibres. Prog. Mater. Sci. **135**, 101089 (2023)
90. K. Mamtani, D. Singh, D. Dogu, D. Jain, J.M.M. Millet, U.S. Ozkan, Effect of acid-washing on the nature of bulk characteristics of nitrogen-doped carbon nanostructures as oxygen reduction reaction electrocatalysts in acidic media. Energy Fuels **32**, 11038 (2018)
91. K. Mamtani, D. Jain, D. Dogu, V. Gustin, S. Gunduz, A.C. Co, U.S. Ozkan, Insights into oxygen reduction reaction (ORR) and oxygen evolution reaction (OER) active sites for nitrogen-doped carbon nanostructures (CNx) in acidic media. Appl. Catal. B Environ. **220**, 88 (2018)